Wind loads prediction using LES: Inflow generation, accuracy and cost assessment for the case of Torre Gioia 22

Wind loads prediction using LES: inflow generation, accuracy and cost assessment for the case of Torre Gioia 22

Jin Xing[a], Luca Patruno[a,], Chiara Pozzuoli[b], Gonçalo Pedro[b], Stefano de Miranda[a], Francesco Ubertini[a]

[a]*DICAM, University of Bologna, Viale del Risorgimento 2, 40136 Bologna, Italy*
[b]*RWDI, Via Thaon Di Revel, 21, 20159, Milano, Italy*

Abstract

In this paper, Large Eddy Simulations, LES, are used in order to evaluate wind loads on a recently designed high-rise building located in Milan, Italy. The selected case study is taken as an example of a typical wind loading assessment, characterized by a complex geometry due to both the shape of the tower and the presence of surroundings. Firstly, the sensitivity of the results to the adopted mesh is analysed. Then, results are compared to wind tunnel measurements and the economical viability of such kind of simulations is discussed. The paper aims at providing an overview of the main factors which can contribute to the success of such analyses and evaluate their accuracy. Not specialized readers will hopefully gain a better insight into the critical aspects which characterize such simulations, while the interested readers will find numerous practical considerations useful for their setup.

Keywords: Wind loading, CFD, High-rise buildings, Large eddy simulation, Aerodynamics

1. Introduction

The use of Computational Wind Engineering, CWE, for the simulation of the wind flow over complex terrains and building arrangements has greatly evolved in the last thirty years, transitioning from early investigations in the research field to widely adopted applications in the design industry [1, 2]. Nowadays, CWE is widely used as an alternative to traditional wind tunnel experiments for applications such as indoor [3] and pedestrian level wind comfort [4] as well as pollutant dispersion [5] and predictions of the flow field in urban areas [6].

With respect to such kind of applications, the evaluation of wind loads on structures

by means of CWE is lagging at least a decade behind: while numerous papers have been presented in the scientific literature [7, 8, 9] demonstrating the suitability of numerical models for such evaluations, their use in practice is still limited and somehow controversial, also due to the heavy legal responsibilities which follow the wind load assessment.

The controversy is fostered by three main aspects. The first one is that wind tunnel tests are built aiming at evaluating at the same time global effects for the design of the main structural systems and cladding loads, usually greatly influenced by local flow mechanisms [10, 11]. It is well-known that the predictive capability of numerical models can be extremely different when targeting such two aspects.

The second one is that numerical models sometimes show a remarkable sensitivity to parameters which might be difficult to be chosen a priori. Such aspect is deeply related to the strong sensitivity to inflow conditions, Reynolds number and geometrical details shown by some cases also in wind tunnel tests: the circular cylinder is only the most well-known member of this infamous family [12, 13]. From this point of view, it might be correctly stated that wind tunnel tests have the inherent advantage with respect to Computational Fluid Dynamics, CFD, simulations to introduce uncontrolled perturbations which are qualitatively more similar to the conditions actually experienced by real flows than the fictitious perfection of numerical models.

The third aspect is actually the most important one and it is inherently intertwined with the two aforementioned points. While it has been repetitively shown that well-resolved scale resolving models can be potentially used for the evaluation of wind loads, for cases characterized by real complexity their cost is still very high, making them only partially competitive with wind tunnel tests. On such regard, it should be added that mesh independence assessments, a cornerstone of numerical simulation, have been often used in the literature in an instrumental way, aiming at producing a measurable proof of the adequacy of the adopted model rather than a methodologically rigorous assessment of the solution quality [14].

In this paper, we present the results of a collaboration between RWDI and University of Bologna for the estimation of wind loads for a newly designed tower denoted Porta Gioia 22,

located in Milan, Italy. The study is aimed at assessing the viability of numerical simulations for the assessment of wind loads in cases characterized by real complexity and taking into consideration computational time/costs constraints. Key aspects of the analyses such as inflow generation and its application to the computational domain are performed with techniques developed by the authors in recent years. Such techniques are here briefly discussed aiming at describing their rationale and highlighting their relations with others methods available in the literature. The analyses are performed aiming at comparing wind tunnel results and numerical simulations in terms of quantities useful for the structural design. We highlight that other similar contributions have been already presented in the literature, usually privileging simple geometries such as the CAARC model, for the sake of reproducibility [15, 16]. In this case we take a different perspective and consider a building characterized by numerous geometrical details [17, 18] taking also into account the reconstruction of the building surroundings. Other contributions with similar characteristics can be found for instance in [19, 20, 8]. Such choice leads only to minor, although fundamental, practical differences with respect to cases characterized by simple geometries, but it leads to completely different choices in the setup of the analyses and in the management of the resources, and thus, on conclusions related to their viability and economical convenience.

The paper is organized as follows: in Sections 2 and 3 the considered case is described and wind tunnel tests used for reference are briefly detailed. The setup used for the numerical simulations is presented in Section 4. Results of the proposed analyses are shown and compared to experimental values in Section 5, where also computational costs are analysed. Finally, conclusions are drawn in Section 6.

2. Case description

The selected case study is part of a vast urban development plan denominated Porta Nuova Gioia, undertaken to modernize an area located in the immediate surroundings of the city centre of Milan. Within the numerous newly constructed buildings, we selected the tower referred to as Torre Gioia 22, designed by César Pelli and under construction at the time of writing.

The tower stands at a height of 120 m, made up of 30 storeys and sits on a three storeys podium. The building is characterized by sharp edges and smooth glass facades, which in some areas are adorned by horizontal decorative elements running along the building corners. The top of the tower is characterized by a crown protected by a 10 m high wall, built on the roof. The building is located in a densely urbanized area, with the presence of other high rise buildings which are already present or planned.

3. Wind tunnel tests

Wind tunnel tests have been performed by RWDI in the boundary layer wind tunnel located in Milton Keynes (UK). The wind tunnel section is 2.4 m wide and 2.1 m high and presents an open chamber testing configuration. The model has been 3D printed at a scale equal to $1:300$, so that the scaled building height is 0.4 m. An overview of the wind tunnel setup is shown in Fig.1 (a). The surroundings of the tower have been modelled in detail within a radius of 360 m (full scale) from the tower, while the main buildings have been reproduced up to a distance of approximately 600 m.

Actually, two configurations of the surroundings have been tested: the first one, denoted as $C1$, is relative to the current condition, while the second one, denoted as $C2$, takes into account the presence of two currently non-existing buildings already planned in the area. In the following, only $C1$ will be considered and reproduced by means of numerical simulations.

The approaching flow has been designed in order to reproduce an Eurocode Category III terrain. The reference height H_r is taken as the building height, H, and the reference velocity there measured in empty wind tunnel conditions is equal to $U_r = 35.8\ m/s$.

The wind tunnel model is equipped with 504 pressure taps acquired synchronously at 512 Hz (see Fig.1 (b)). For each configuration (i.e. $C1$ and $C2$), the incidence angle is varied with increments of 10° and pressures are recorded for 35 s. Before postprocessing, a low-pass filter with cut-off at 128 Hz has been applied.

Assuming a design wind speed equal to 30 m/s at the tower height, the acquired time-series correspond to approximately 210 min in real scale, so leading to 21 $10-min$ samples.

(a) (b)

Fig. 1. Overview of the setup used for wind tunnel tests: (a) surroundings and (b) detail of the tower.

4. Numerical model

In the following, the numerical model used to perform the analyses is described. The components and modelling choices which contribute the most to the effectiveness of the simulation and/or to the quality of the obtained results are discussed in detail. Indeed, as it will be later further discussed, some choices operated in the model setup are known to be sub-optimal and are dictated by the need to ensure the robustness of the simulations and their actual viability (in terms of stability and computational requirements) in complex cases. Simulations have been performed with OpenFoam v6 using the infrastructures of CINECA (Consorzio Interuniversitario dell'Italia Nord Est per il Calcolo Automatico), Italy.

4.1. Computational domain

An overview of the computational model, realized at the same scale used for wind tunnel tests, is provided in Fig. 2. The computational domain measures 5.0 m, 3.5 m, and 2.1 m in length, width and height, respectively. The distance from the inlet patch to the tower is 2 m.

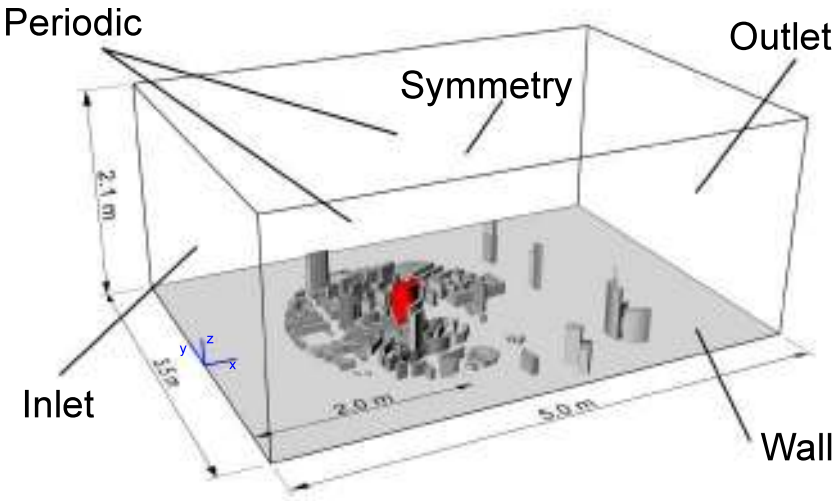

Fig. 2. Overview of the computational domain and the adopted boundary conditions.

Actually, in order to facilitate the meshing operations, in analogy with wind tunnel procedures, a rotor-stator approach is adopted. In particular, the computational domain is subdivided into two zones: a cylinder of radius 1.3 m with axis oriented along the z-direction passing through the tower centre (denoted as rotor in the following) and all the rest of the domain (denoted as stator in the following). The two parts are connected by a non-conformal interface. A view of the rotor geometry is provided in Fig. 3 (a) while a detailed view of the tower is provided in Fig. 3 (b). The geometry of the tower has been rebuilt starting from that exported from the architectural model but defeaturing has been limited to extremely small details and mainly used to eliminate unnecessary edges between surfaces partitions, which strongly jeopardize the results of the meshing operations.

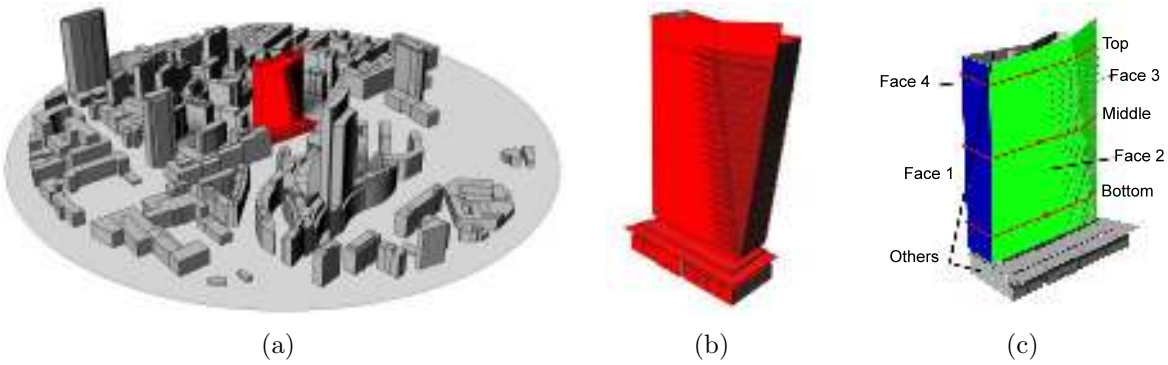

(a) (b) (c)

Fig. 3. Detailed views of the studied geometry: (a) rotor, (b) tower and (c) paths and faces adopted to present results.

When studying the wind effect at different angles of attack the rotor part is rigidly rotated while the stator part is re-meshed, because it includes some of the buildings. Considering that the meshing operations are particularly delicate and time-consuming exclusively for the rotor, the approach maintains its convenience despite the fact that the stator must be re-meshed for some angles. On such regard, it should be noticed that enlarging the rotor to avoid such problem is not advisable, as it leads to a large number of cells. This is due to the fact that the rotor must be meshed in a uniform manner, without taking advantage of the wind directionality. Finally, it should be noticed that meshing has been here performed using SnappyHexMesh, the standard meshing tool included in OpenFoam which uses a top-down approach. When using such tool it should be bear in mind that the quality of the obtained mesh is sensibly affected by the orientation of the geometry with respect to the starting mesh. It is thus advisable to mesh the rotor part aligning the building geometry with the reference system whenever possible, especially when relatively coarse meshes are adopted.

4.2. Mesh

An overview of the mesh is provided in Fig. 4 (a) while a detail view of the tower is provided in Fig. 4 (b). The volume inside the rotor is meshed with a size approximately equal to $0.04H$ (5 m in full scale). The buildings composing the surroundings are meshed with a typical size equal to $0.02H$ (2.5 m in full scale) and this size is adopted up to a distance from their surface equal to $0.125H$. The surrounding buildings edges are meshed

with a typical size equal to $0.01H$ (1.25 m in full scale), the same used for the tower surfaces and for the volume close to the tower up to a distance equal to $0.25H$. The tower edges, the decorative details projecting from the facades and the crown of the tower are meshed with a typical size equal to $0.005H$ (0.62 m in full scale). An expansion ratio is adopted in the vertical mesh spacing in order to obtain a coarser mesh moving away from the ground. The adopted expansion ratio is such that cells at the top of the domain are three times larger than those at the ground.

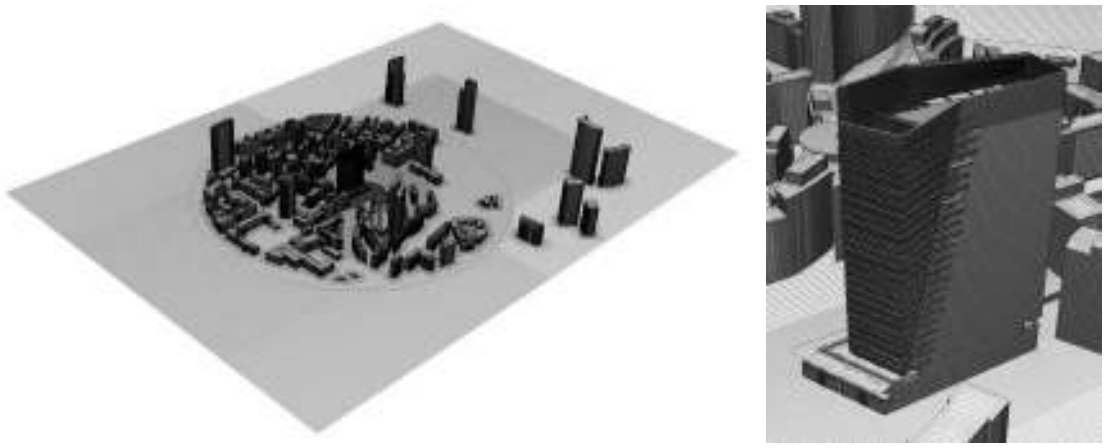

(a) (b)

Fig. 4. The adopted mesh: (a) overall and (b) detail of the tower.

As it can be seen from Fig. 4 (b) some details of the tower cannot be meshed with a good resolution using such mesh sizes. Although an overall good result is obtained, some of the edges could not be meshed accurately. This is particularly true for small details and thin walls located on the crown. The effects of such geometrical inaccuracies can be dramatic in smooth flow conditions but might be moderate in strongly turbulent flows and must be evaluated based on the obtained results.

The stator is meshed with the same sizing used for the rotor in the zone extending from the ground up to an height equal to $2.5H$ in the zone upstream the rotor. The same sizing is also used in the zone downstream the rotor, up to a distance equal to 5 H from the tower. The other parts are meshed with the coarser adopted mesh level, characterized by size in the xy-plane equal to $0.08H$. A refinement has been adopted also at the rotor-stator interface

to reduce the errors introduced by the non-conformal interface. Overall, the maximum non-orthogonality is equal to 70° and it is concentrated in an extremely limited number of cells. Analogously the maximum skewness is equal to 5.

The mesh obtained by adopting such sizings counts in total 9.5 M cells. We notice that we did not introduce boundary layers to perform the simulations. The normalized wall-distance $y+$ around the tower surface is 10 on average and the maximum value is around 100. Indeed, their introduction would strongly increase the cell count and, willing to keep fix the total number of cells, would require to coarsen the mesh in the building surroundings. On such regard, it is noticed that in the literature there is a consolidated tendency to consider y^+ a fundamental parameters to judge mesh quality. In fact, this is well-justified for streamlined bodies, especially when immersed in smooth flows (and in fact its importance is well-justified for aeronautical applications). However, it is indeed unclear why such parameter should be considered of paramount importance for bluff-bodies with sharp corners immersed in turbulent flows. The overall result is that, in order to obtain a low y^+, most of the time the mesh is rapidly coarsened in the zones occupied by detached shear layers, which are actually among the most important flow features for bluff body aerodynamics [21]. We also notice that the presence of perfectly sharp edges have been found to be problematic from the numerical point of view leading to paradoxical results [13], which might be worsened by mesh refinement at edges and corners.

In a summary, the 9.5 M cells are subdivided so that approximately 7 M are in the rotor and approximately 2 M are in the immediate surroundings of the tower.

4.3. Models and numerical schemes

The standard $k-$*equation* LES model [22] is adopted in order to model subgrid stresses together with Van Driest damping functions at wall-boundaries. Bounded linear schemes are adopted to evaluate fluxes at the cell faces for all quantities apart from velocities, for which the LUST scheme is adopted [23]. Gradients and laplacians are calculated using partially corrected schemes, in which the non-orthogonal part is forced to be smaller than the orthogonal part. Such choices, as it is well-known, sacrifices accuracy favoring numerical

stability. PISO is adopted for pressure-velocity coupling. The pressure field is solved using the GAMG solver while a symmetric Gauss-Seidel smoother is used for the velocity field. Tolerances are set to 10^{-5} for all quantities apart from the final pressure for which 10^{-6} is adopted.

The Crank-Nicolson scheme with 10% backward Euler scheme is used for time advancement with a non-dimensional time step $\triangle t \cdot U_r/H \ = 2.2 \cdot 10^{-3}$ (where U_r is 11.3 m/s and H is the building height), leading to a maximum Courant number equal to 4 only in some particularly small cells and well-below 1 in the immediate building surroundings.

4.4. Boundary conditions

An overview of the boundary conditions, BCs, adopted for the current case is provided in Fig. 2. In particular, wall conditions are adopted for the tower surfaces, the surroundings and the ground. Periodic conditions are adopted for the sides (a larger domain with respect to the wind tunnel section is used, also considering the open chamber configuration) and symmetry conditions are used for the top. The rotor and the stator are connected using a non-conformal mesh interface and a mixed inlet-outlet condition is adopted at the outflow.

As it can be noticed, the fetches located in front of the tower in the wind tunnel tests have not been reproduced. It is thus mandatory to adopt a turbulent inflow in order to reproduce the incoming Atmospheric Boundary Layer, ABL, profile. In this case, the inflow condition has been specified in agreement with wind tunnel tests as regards the time-averaged wind speed and turbulence intensity for the along wind velocity components. Other quantities have been estimated based on empirical relations found in [24, 25, 26]. The unsteady inflow condition has been obtained through the generation of synthetic turbulence according to [27] and as it is further detailed below.

4.5. Synthetic turbulence

It is well-known from wind tunnel tests that a correct reproduction of the incoming unsteady velocity field expected on site is of fundamental importance for the evaluation of wind loads [28, 29]. In the present study the surroundings of the tower are explicitly modelled but,

also in these circumstances, the incoming ABL should be accurately reproduced, because the explicitly modelled surroundings are relatively small if compared to the distance needed to allow the development of the ABL. Additionally, the large turbulence scales are the ones which contribute the most to the definition of the wind loads, but are also the ones which require longer fetches to be produced. In wind tunnels, the distance needed for their development is usually shortened by adopting spires [15, 8]. Additionally, in CWE computations the introduction of inflow turbulence has the role to destabilize shear layers produced by the surroundings, which are usually only roughly meshed and, thus, are excessively stable with respect to the real ones.

In the last years, the generation of synthetic turbulence to be used as inflow condition for scale resolving simulations and at the interface between hybrid models has been the object of numerous researches [30, 31]. Briefly, available methods can be grouped into the following groups:

(a) Simulation Assisted inflow generation methods (*SA*, in the following);

(b) Synthetic Generation without or with partial approximation of the governing equations (*SGwo*);

(c) Synthetic Generation with approximation of the governing equations (*SG*).

In the present simulations the incoming flow is generated relying on the PRFG^3 method which is of the *SG* type for homogeneous flows while it becomes of *SGwo* type for strongly non-homogeneous flows (as most of the available *SG* methods). We invite the reader to refer to [32] for details and to [27] for its use in the context of ABL generation. Additional details regarding the generation of inflow conditions and an overview of the available methods is provided in Appendix A.

Briefly, PRFG^3 relies on a complete four-dimensional spectral decomposition of the velocity field in order to ensure the matching of the three target turbulence intensities (one for each velocity component) and a good approximation of the nine targeted integral length scales. The method takes into account the realizability conditions of a divergence-free velocity field and the convection operated by the time-averaged velocity.

Once the synthetic field has been generated, it must by applied to the numerical simulation. Such operation is not trivial as pressure fluctuations often arise. Further details on the application of unsteady inflow conditions can be found in Appendix B. In the present work velocity fluctuations are applied at the inflow patch using the Variationally Based Inflow Correction, VBIC, method [33].

Using the aforementioned procedure, the inlet turbulent field is generated targeting an Eurocode Category III profile, indicated as Tar. in Fig. 6. The mean velocity and along-wind turbulence intensity, I_u, follow the Eurocode prescriptions, while I_v and I_w are $0.75 \cdot I_u$ and $0.5 \cdot I_u$, respectively. Consequently, the reference velocity, U_r, is 11.3 m/s at H_r, where the turbulence intensities in the x, y and z directions are approximately 20%, 14% and 10%, and the integral length scales for u, v and w in the along-wind direction are 150 m, 54 m and 30 m in real scale, respectively.

5. Results

In the following, results obtained using the previously described computational model are reported. Firstly, the impinging wind profiles are discussed and compared with wind tunnel data in Sec. 5.1. Then, in Sec. 5.2 the sensitivity of the results with respect to the adopted computational mesh is analyzed. Results obtained by varying the wind angle of attack are reported in Sec. 5.3. Assessments regarding design values such as global forces and peak pressures are shown in Sec. 5.4 and Sec. 5.5. Finally, computational costs are discussed in Sec. 5.6. It is remarked that time histories obtained with numerical simulations have been treated with a low-pass filter according to wind tunnel results.

5.1. Inflow

A qualitative overview of the obtained velocity field is provided in Fig. 5. The vortical structures generated at the inflow can be clearly distinguished in Fig. 5 (a). The variation of the eddy size, which increases moving away from the ground, can be also clearly noticed. In Fig. 5 (b) the vortical structures produced in the proximity of the tower are detailed.

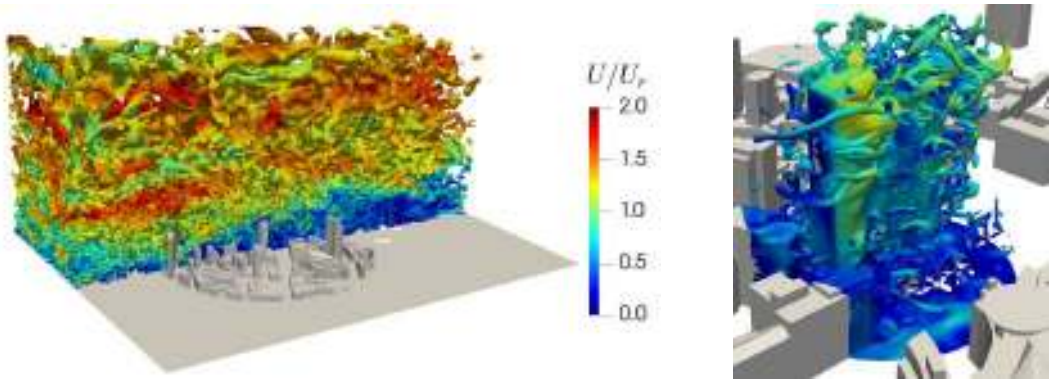

(a) (b)

Fig. 5. Overview of the velocity field: (a) overview of Q-isosurfaces ($Q(H_r/U_r)^2$=0.26) and (b) detail of vorticity ω-isosurfaces (($\omega(H_r/U_r)$=30)). Both are colored by instantaneous velocity magnitude.

For checking the results produced by the inflow generation procedure, an empty computational domain without any obstacle is firstly simulated. A comparison between the velocity and turbulence intensity profiles measured in the wind tunnel, the ones targeted by the synthetic turbulence generation procedure and those actually obtained in the simulation is reported in Fig. 6 (a) and (b). In order to characterize the along wind evolution of the velocity field, 12 profiles arranged on a grid located between the inflow patch and the location where the building will be placed (the origin of the reference system) are considered (uniformly spanning the intervals $x \in [-500, 0]$ m and $y \in [-300, 330]$ m, full-scale). Then results are represented considering the envelope of such profiles and their mean value. Analogously, the profiles of the along-wind integral length scales for all velocity components is also reported in Fig. 6 (c), but in this case comparison is provided with the target value used for L_{ux}, calculated in agreement with [26]. Overall a well-satisfactory agreement between the three can be observed.

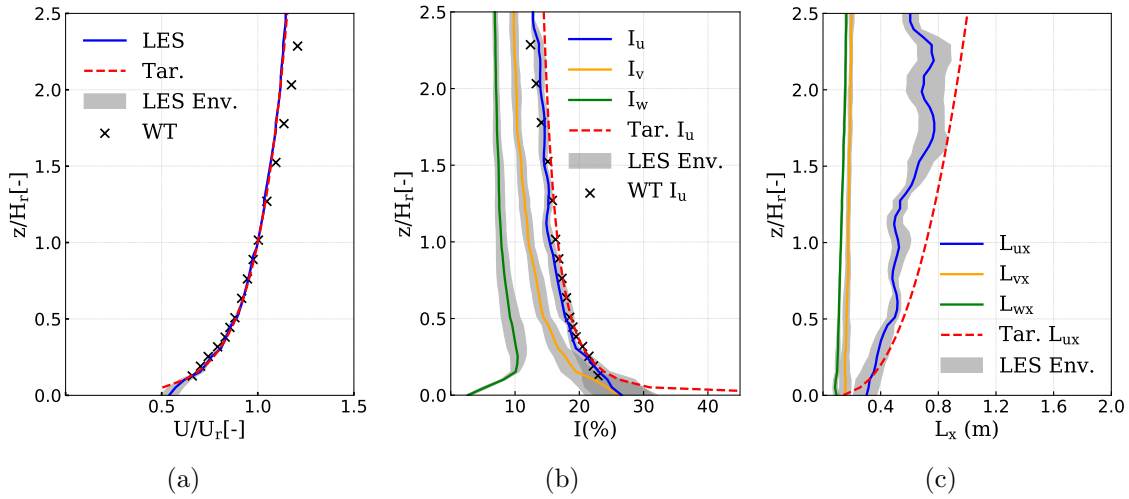

(a) (b) (c)

Fig. 6. Velocity profile: (a) time-averaged velocity, (b) turbulence intensities, (c) along-wind integral length scales.

The spectra of the three velocity components measured at a distance of 0.5 m from the inflow patch and at the building location at H_r are shown in Fig. 7. As it can be observed a good agreement with the target values used in the synthetic turbulence generation procedure has been achieved.

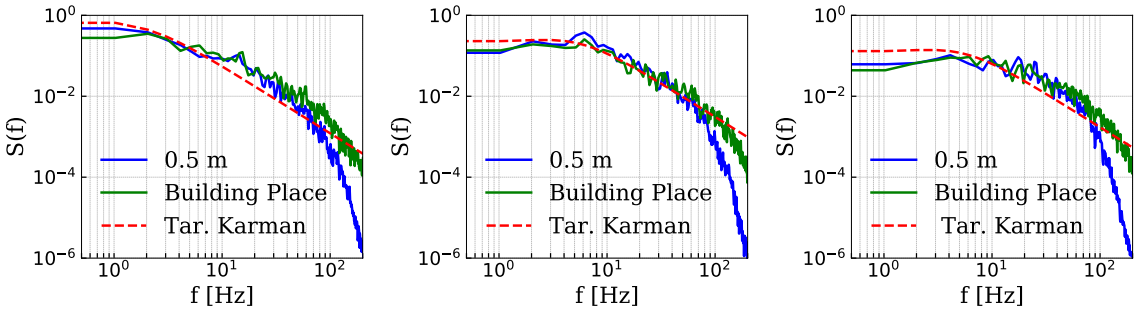

(a) (b) (c)

Fig. 7. Spectra of the velocity components measured at a distance of 0.5 m from the inflow patch and the building location at the height of H_r: (a) along-wind component, (b) cross-wind component and (c) vertical component.

5.2. Mesh sensitivity

In this section, the sensitivity of the results to the mesh sizing is analyzed. As anticipated, in the authors' opinion mesh independence is a vague concept for scale resolving simulations,

which must be detailed according to the intended use. We thus proceed, as many others, using it instrumentally in order to assess the effect of the grid on the obtained results. From this point of view it appears more appropriate to speak about mesh sensitivity rather than mesh independence.

In particular, three meshes have been considered. The first one is that described in Sec. 4.2 and, in the following, it is denoted as *Mesh M*. As previously reported, it is characterized by approximately 9.5 M cells and mesh sizing equal to $0.01H$ close to the building surfaces and inside the volume up to a distance equal to $0.125H$ from the tower surfaces. Some parts of the tower in which smaller geometrical details are present are meshed with a sizing equal to $0.005H$.

Then, two additional meshes are considered. In particular, a coarse grid, denominated *Mesh C* is also adopted. The mesh is composed of approximately 3.0 M cells. It has been obtained by a global coarsening of the mesh (also in the rotor part) and by considering a typical mesh size close to the tower equal to $0.015H$. When such mesh is adopted, the tower edges and geometry can be only roughly approximated, especially when a top down approach is used for meshing.

The last considered mesh is denominated *Mesh F* and represents a finer version of *Mesh M*. In particular, the surroundings are meshed using the same settings used for *Mesh M* but all the tower surfaces are meshed with size $0.005H$ and such dimension is used also inside the fluid domain up to a distance equal to $0.25H$. The mesh counts approximately 20 M cells.

Figure 8 reports a scatter plot of the results obtained by using the three aforementioned meshes against experimental measurements at null angle of attack for all the monitored pressure taps. In particular, Fig. 8 (a) reports the time-averaged pressure coefficient, $\bar{C}_p$, while Fig. 8 (b) reports the pressure coefficient standard deviation C'_p. It can be seen that all three meshes lead to good predictions of the time-averaged values, so that the scatter plot is mainly located in the proximity of the bisector. A few outliers are present for which all the three meshes lead to the same predictions, suggesting that such values might be influenced

by slight discrepancies between the physical and the numerical model. As expected, the main effect of refining the mesh is observed for low pressure zones, located in the proximity of the edges, for which *Mesh F* leads to slightly better results (due to the fact that a fine sizing is used for all the building surfaces). Looking now at C'_p, as expected, a larger scatter is observed, the coarse mesh leads to both under and over-estimations, so that it is difficult to reach final conclusions regarding the adequacy of the three investigated meshes.

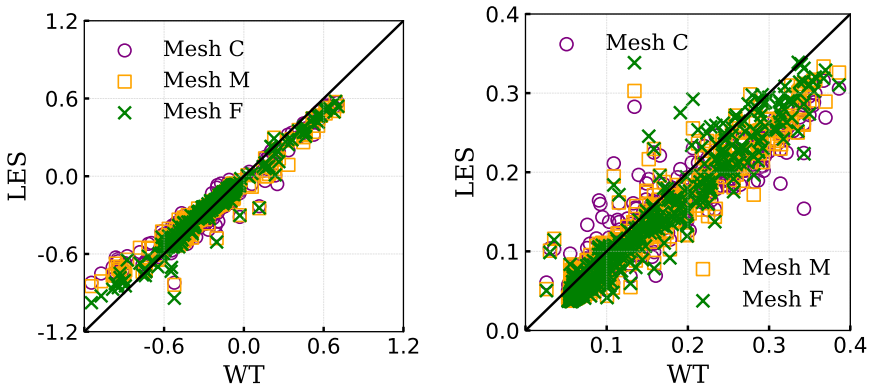

(a) (b)

Fig. 8. Scatter plot of C_p statistics at 0° angle of attack for the three considered meshes: (a) $\bar{C}_p$ and (b) C'_p.

We now investigate the dependency of extreme pressure values on the adopted mesh size. In particular, as anticipated, wind tunnel time-histories are representative of 21 samples of duration equal to 10 min in real scale. We thus proceed by fitting a Gumbel distribution using the method of moments to such extreme values, so allowing to define the corresponding 90% probability confidence interval. We then plot the extreme values measured in the numerical simulations and compare them with the aforementioned confidence interval. Figure 9 reports for 10-min maxima (and minima) the confidence interval obtained using wind tunnel tests for each probe, as well as the 10-min extreme (a single value) measured in the numerical simulations using *Mesh C*, *Mesh M* and *Mesh F*, respectively. When plotting such results, for the sake of clarity of the representation, the probes have been reordered in ascending (descending for minima) value of the mean 10-min extremes extracted from wind tunnel tests.

It can be seen that results obtained in the numerical simulations are in reasonable agreement with experimental values but differences emerge at the most critical probes, characterized by highest suctions. Here *Mesh C* appears to systematically underestimate peak suctions, which do not exceed the value of approximately -1.5, to be compared to the -2.5 measured for *Mesh F*. The situation is summarized in Table 1. It can be seen that for *Mesh C* values extracted from the simulations are inside the 90% confidence interval 48.1% and 61.3% of the times for maxima and minima, respectively. Such values are in the range 70%-80% when *Mesh M* and *Mesh F* are adopted, without a monotonic increase of the score with the mesh refinement. Notice that a perfect match would be obtained when the values measured in the numerical simulations are within the confidence interval 90% of the time (also the fact that pressure extreme values do not perfectly respect the Gumbel distribution contributes to lower the obtained score).

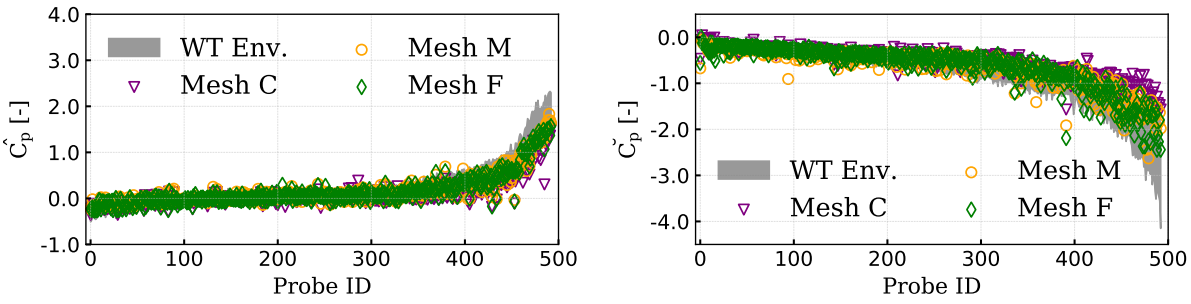

Fig. 9. Comparison of peak prediction among three mesh sizes: (a) maxima and (b) minima.

Table 1
Sensitivity of the results with the adopted mesh size: extreme values from numerical simulations falling within the 90% probability interval obtained from wind tunnel tests.

	Mesh C	Mesh M	Mesh F
Maxima [%]	48.1	74.8	73.0
Minima [%]	61.3	77.3	71.6

To further investigate the distribution of the 10-min extremes, the cumulative density function of the obtained values is reported in Fig. 10 and 11 (accumulation over all the monitored pressure taps). In particular, for wind tunnel the cumulative density function is

calculated base on the extremes which has 50% probability of exceedance while, for numerical simulations, it is calculated based on the single available realization. As expected, for *Mesh C* discrepancies are observed over an extended range of pressure values: for suctions a much more rapid decay of the distribution on the negative side with respect to wind tunnel is observed. For *Mesh M* a much better agreement is observed and differences are concentrated in the high suction zones. *Mesh F* leads to a very good agreement also for strong suctions. It should be anyway noticed in Fig. 9 that, for very strong suctions, simulations tend to provide values systematically falling in the higher part of the confidence interval calculated basing on wind tunnel results, in practice leading to results not on the safe side.

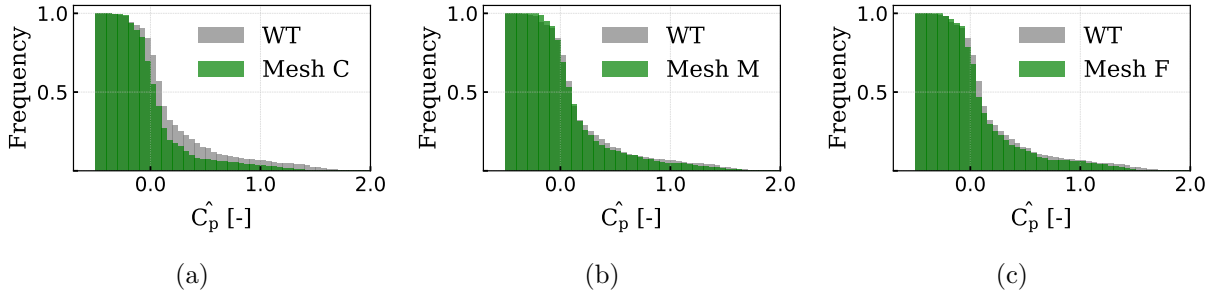

Fig. 10. The distribution of $\hat{C}_p$ for different meshes: (a) *Mesh C*, (b) *Mesh M* and (c) *Mesh F*.

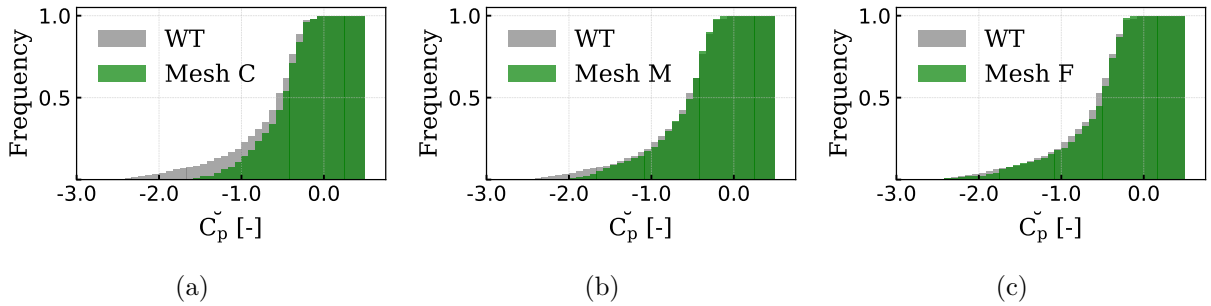

Fig. 11. The distribution of $\check{C}_p$ of different meshes: (a) *Mesh C*, (b) *Mesh M* and (c) *Mesh F*.

In conclusion, it appears that *Mesh C* provides sensibly different results with respect to the wind tunnel for many quantities of interest. Some differences are also recorded for *Mesh M* and *Mesh F* for peak values, especially for 10-min extreme suctions but results do not appear to clearly ameliorate with refinements of the zone in the proximity of the tower. In

the following only *Mesh M* is considered in order to perform simulations at other angles of attack.

5.3. Polar

The instantaneous flow field in the proximity of the tower at 0°, 120° and 240° is qualitatively depicted in Fig. 12.

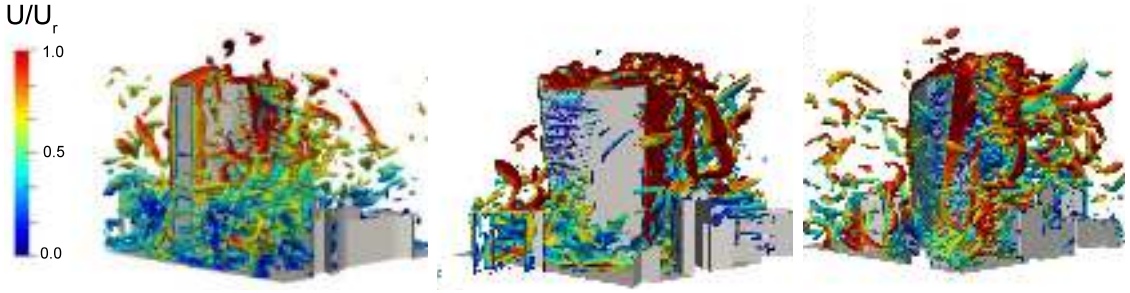

(a) (b) (c)

Fig. 12. Instantaneous flow field at different attack angles: (a) 0°, (b) 120° and (c) 240°.

Figure 13 reports the distribution of C_p along three paths which go around the building at three heights (see Fig. 3(c)) at null attack angle. In particular, the time-averaged value and the standard deviation are considered. The coordinate along the path is indicated as s.

Overall, a good agreement between experimental results and simulations is observed. As expected, at the edges between inclined faces, a sharp change in the pressure field is observed, with the formation of jumps and cusps at the passage between differently oriented faces. Such jumps and the prominence of the cusps, as expected, is slightly underestimated in the simulations.

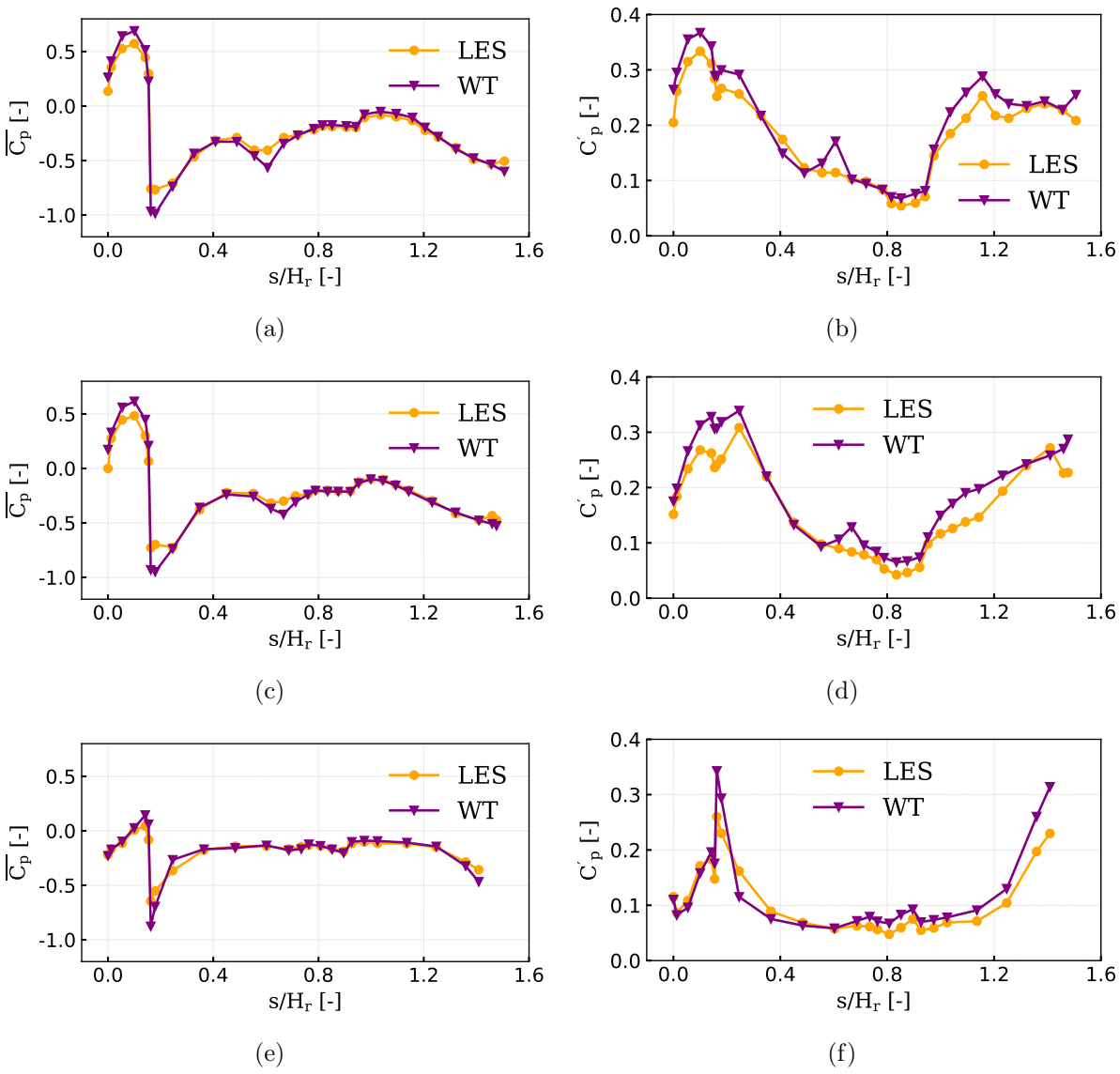

Fig. 13. Pressure coefficient statistics at 0° angle of attack: (a) $\bar{C}_p$ and (b) C'_p for Top path, (c) $\bar{C}_p$ and (d) C'_p for Medium path, (e) $\bar{C}_p$ and (f) C'_p for Bottom path.

Figure 14 shows the distribution of the C_p time-average and standard deviation for the angle of attack 240°, which correspond to a wind perpendicular to the long building side. Results qualitatively confirm those obtained for 0°, although in this case a systematic underestimation of the time-average and standard deviation of pressure is observed. Given the complexity of the model it is difficult, and probably not useful, to detail the cause of the discrepancies. Nevertheless, as those are observed on the face of the building directly hit

by the incoming wind, it might be conjectured that they are related to differences in the impinging turbulent structures produced by the surrounding buildings.

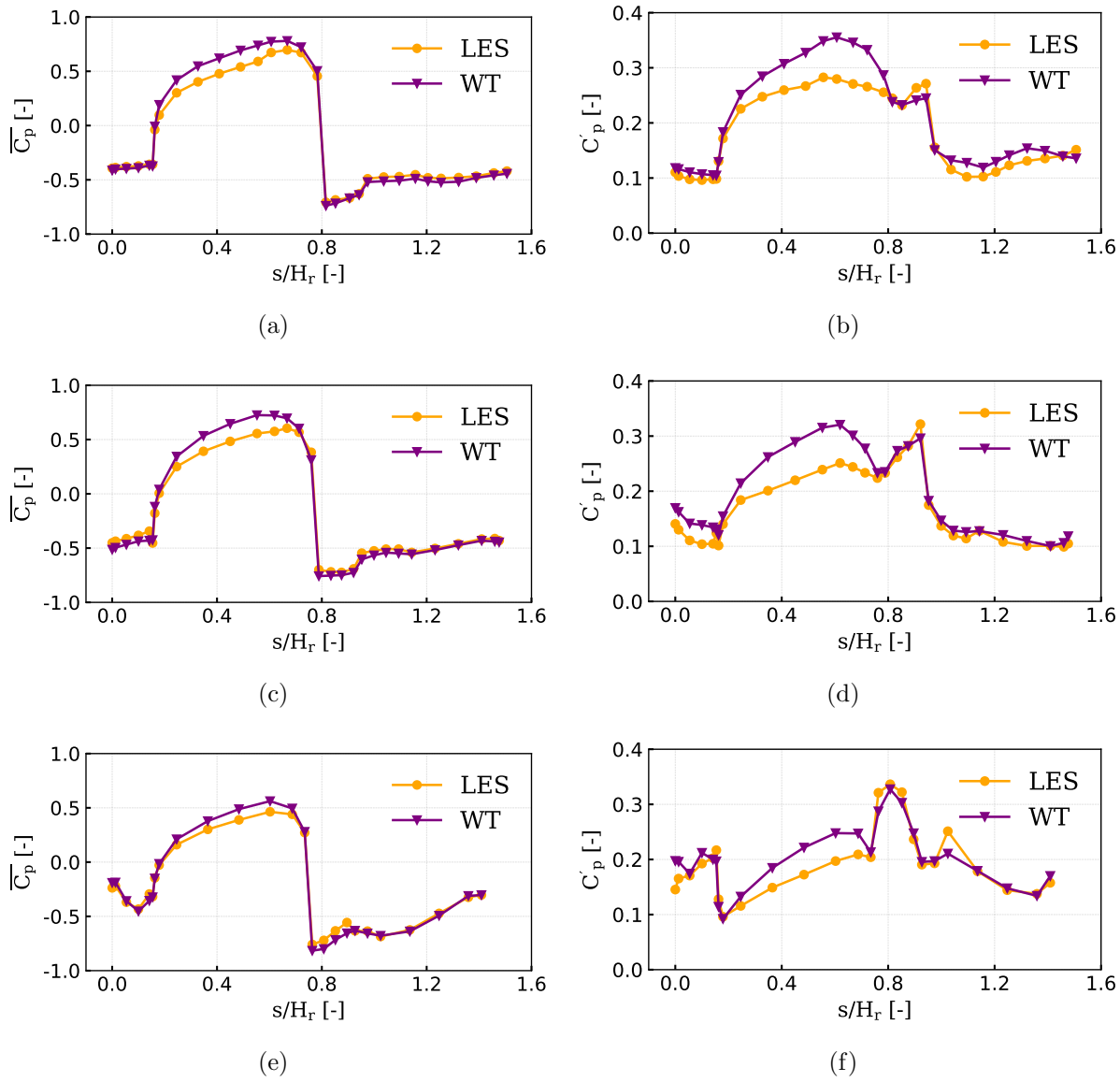

Fig. 14. Pressure coefficient statistics at 240° angle of attack: (a) $\bar{C}_p$ and (b) C'_p for Top path, (c) $\bar{C}_p$ and (d) C'_p for Medium path, (e) $\bar{C}_p$ and (f) C'_p for Bottom path.

In order to provide a global overview of the obtained results, scatter plots which related experimental measurements and simulation results are proposed in Fig. 15 and 16. Here six angles of attack, equally distributed along all possible directions, are considered. Results are presented using different markers to allow to identify the face (see Fig. 3(c)) to which

pressure taps belong. The coefficient of determination, R^2, of experimental and numerical data is reported in Table 2.

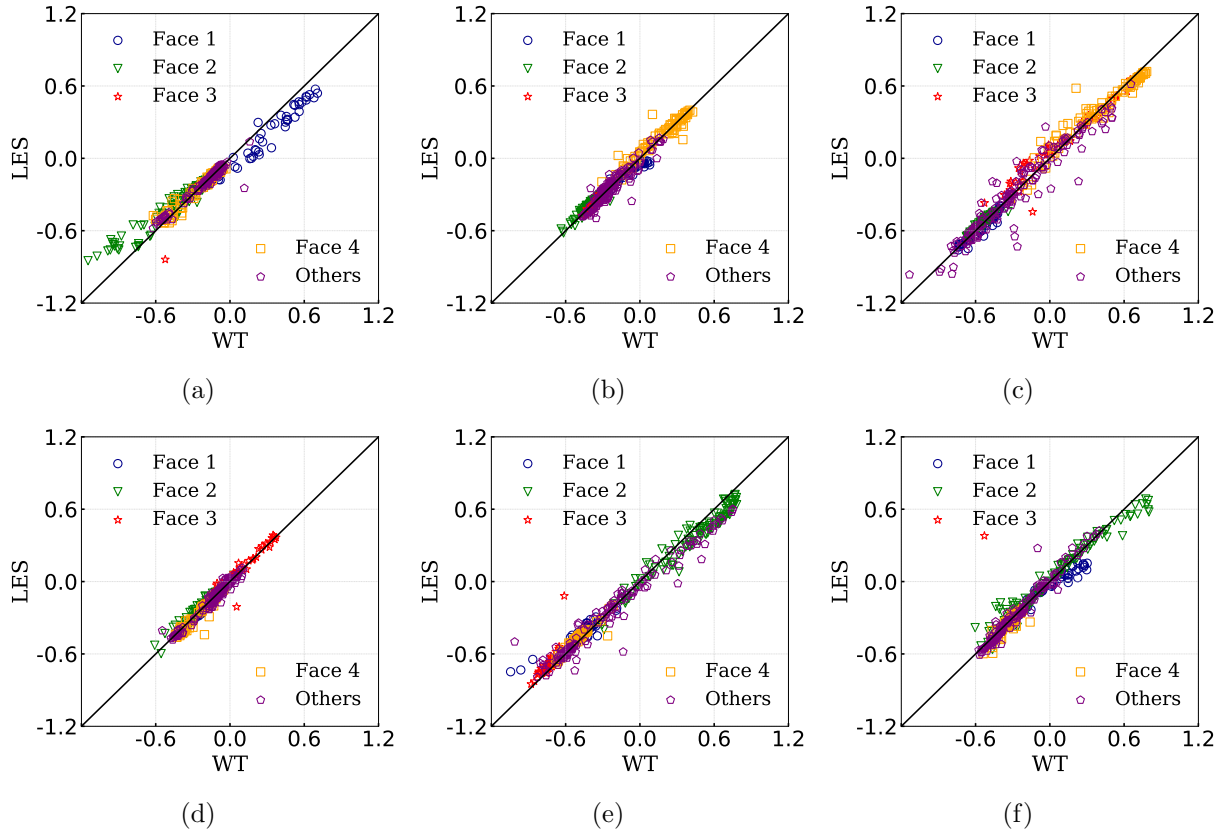

Fig. 15. Scatter plots of $\bar{C}_p$: (a) 0°, (b) 60°, (c) 120°, (d) 180°, (e) 240° and (f) 300°.

Analogously, for the pressure coefficient standard deviation, results are presented in Fig. 16. Also in this case, R^2 is reported in Table 2.

Table 2
Coefficient of determination, R^2, of each wind angle of attack.

	0°	60°	120°	180°	240°	300°	Mean
$\bar{C}_p$	0.95	0.93	0.90	0.92	0.96	0.91	0.93
C'_p	0.92	0.89	0.70	0.92	0.78	0.87	0.85

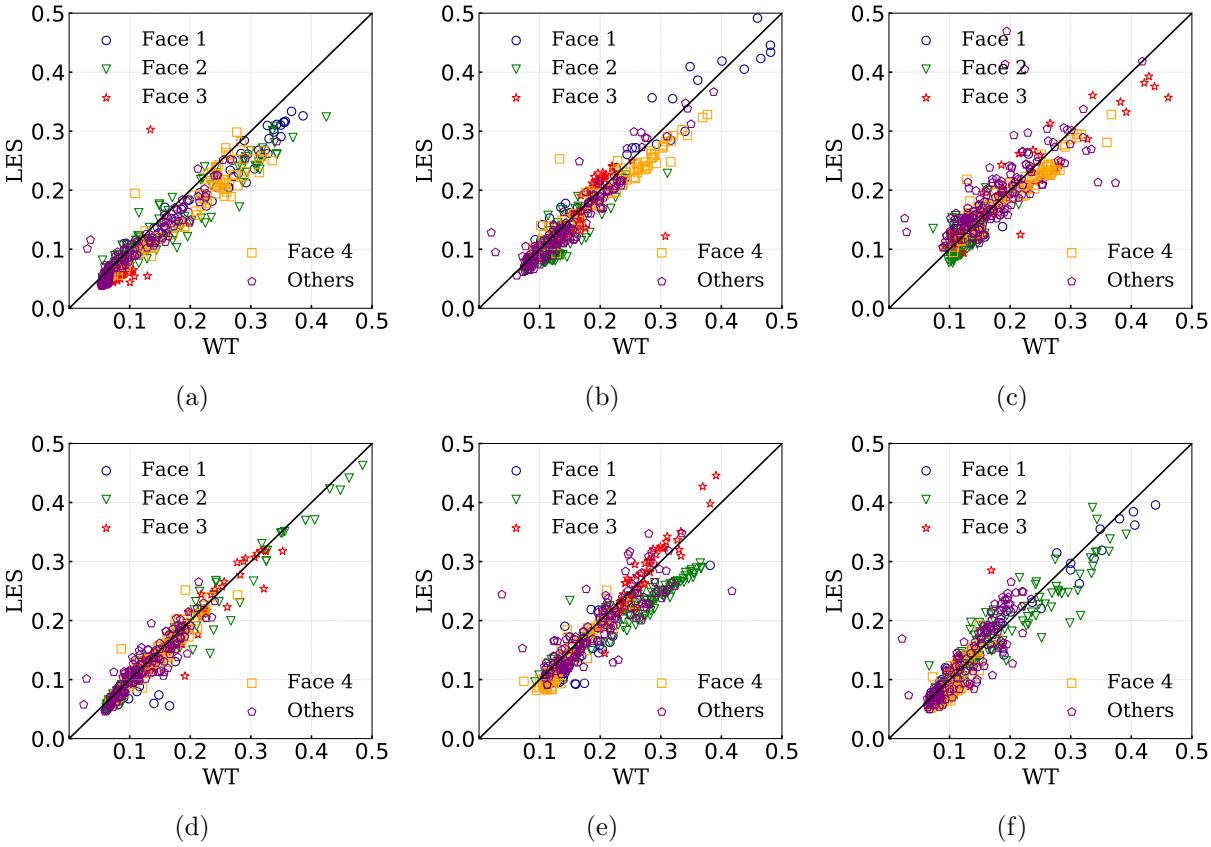

Fig. 16. Scatter plots of C'_p : (a) 0°, (b) 60°, (c) 120°, (d) 180°, (e) 240° and (f) 300°

5.4. Global forces

Up to now we provided an overview of the first and second order pressure statistics distribution. Here we provide an assessment regarding the accuracy of global forces, expressed in terms of aerodynamic coefficients based on the tower height. In particular, forces have been calculated by integrating the pressure field, so leading the forces time-histories. Then, for each angle of attack, the mean value and peak design values have been extracted assuming a Gumbel distribution for the extremes. Quantiles associated to 90% probability have been extracted for wind tunnel data while the extremes for numerical simulations are extracted directly from the time history. Results are shown for each force (moment) in Fig. 17 showing very good results in terms of time averaged values and a very good reproduction of the envelope shape for almost all angles of attack. We notice a relatively large discrepancy for the simulation at 300° which further inspection revealed to be caused by a single event recorded

within the simulation.

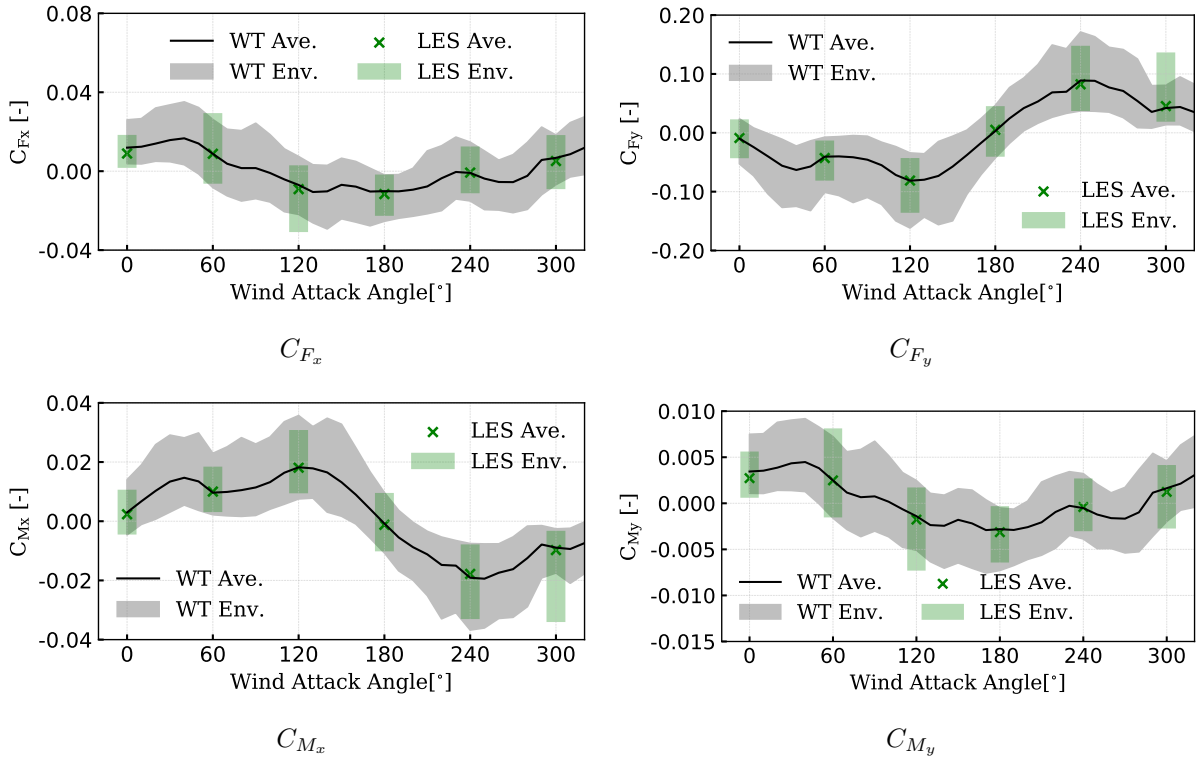

Fig. 17. Comparison between experimental and simulated global forces and moments.

5.5. Peak pressures

Similarly to what has been done in Sec. 5.2, we now proceed to analyse the extreme values from all considered angles of attack. Results are summarized in Fig. 18 as regards maxima and in Fig. 19 as regards minima. Also in such plots the numbering of the pressure taps have been changed for the sake of clearness, ordering them in ascending order with respect to the wind tunnel mean extreme value (maximum and minimum respectively).

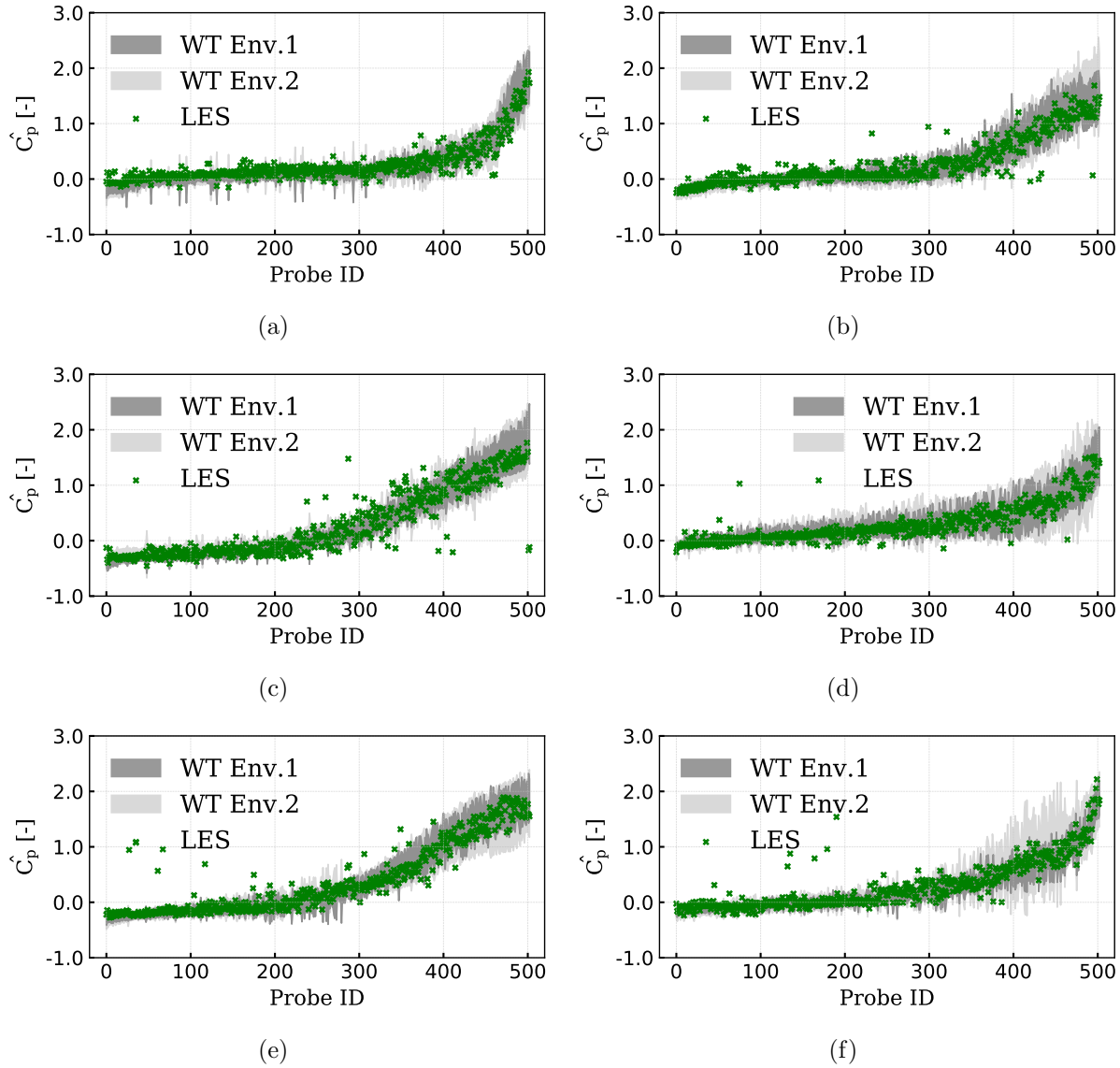

Fig. 18. Maximum predicted C_p: (a) 0°, (b) 60°, (c) 120°, (d) 180°, (e) 240° and (f) 300°

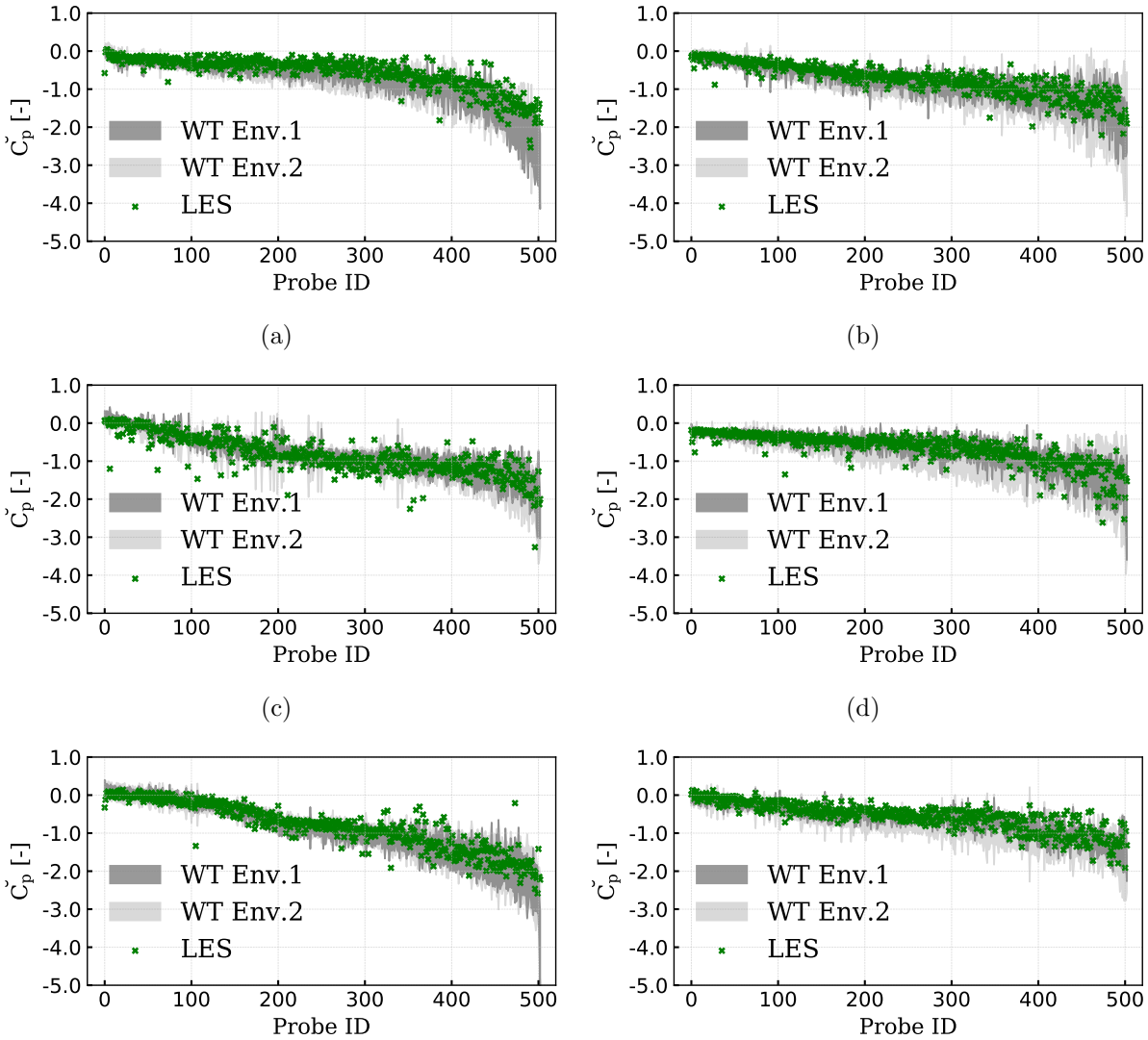

Fig. 19. Minimum predicted C_p :(a) 0°, (b) 60°, (c) 120°, (d) 180°, (e) 240° and (f) 300°

In this case, data are compared with two envelopes extracted from wind tunnel data. In particular, *Envelope 1* is extracted from the 10-min extremes measured in wind tunnel tests (Gumbel distribution, 90% probability). As regards *Envelope 2*, it is obtained by calculating 90% probability 10-min extremes for the considered angles and incrementing it of ±10°. This is done in order to qualitatively evaluate if a small change in the angle of attack can be considered responsible for the observed discrepancies.

Table 3 reports the percentage of extremes falling within the previously calculated confi-

dence interval for all the considered cases. As it can be seen, results previously presented are confirmed. The numerical simulations fall inside the calculated *Envelope 1* type confidence interval an average of 80% of the times. When *Envelope 2* is considered, the scores is in the order of 90 %. Despite those error metrics, it should be anyway noticed that numerical results tend to accumulate in the lower zones of the calculated confidence intervals. This is particularly evident for Fig. 19 (a) and (e), for which, at high suctions, the peak values measured in the simulations tend to cumulate at milder suction values. On such regard, further research is needed as the evaluation of peak loads by means of numerical simulation, despite its importance, has not been deeply investigated in the literature.

Table 3
The percentage of extremes falling in the WT confidence interval.

Peak types		0°	60°	120°	180°	240°	300°	Mean
Maximum	Inside Env.1 ratio (%)	74.8	84.9	68.0	87.3	80.7	69.8	77.6
	Inside Env.2 ratio (%)	87.5	91.8	84.7	95.0	93.0	90.3	90.4
Minimum	Inside Env.1 ratio (%)	77.3	88.3	75.1	87.1	80.9	75.7	80.7
	Inside Env.2 ratio (%)	88.5	94.4	86.5	94.6	91.3	86.7	90.3

5.6. Computational costs

In this section the computational costs involved in running the proposed simulations are detailed and the budget for a complete study is discussed.

The proposed simulations have been run at CINECA, on the GALILEO supercomputer, which is equipped with 1022 nodes each composed of 2x18-core Intel Xeon E5-2697 v4 (Broadwell) at 2.30 GHz. Running each simulation with a number of cores comprised between 100 and 200, each simulation required approximately 5000 *Core-h* to complete for the *Mesh M* 10 min in real scale, which should be considered a minimum requirement in agreement, for instance, with [34].

Although in the present study, for the sake of convenience, simulations have been performed every 60°, a stepping comprised between 10° and 30° is usually required [34]. Assuming for instance to sample the attack angle every 30°, this requires 12 simulations to complete the attack angles.

It is thus easily possible to see that a complete study performed as described in this paper requires approximately 6.0E4 *Core-h* if every angle of attack is sampled for 10 mins, while it would require 3.6E5 *Core-h* for a 1 *h* sample in full-scale, from which a more careful evaluation of the extreme values can be obtained.

According to [35, 36], we here assume a cost of the *Core-h* equal to 0.1 euro (this might be considered an average value with typical oscillations of about 20%). This leads to a total cost comprised between 3k and 50k euro, which is indeed the range of price of wind tunnel tests.

It is nevertheless noticed that the cost structure of wind tunnel tests and numerical simulations is completely different: the fist ones are characterized by fixed costs due to the wind tunnel infrastructure and the model production and installation, being the actual tests relatively quick and inexpensive. On the other side, CFD is characterized by relatively low fixed costs for the simulations setup, while variable costs increase linearly with the simulation time and the number of studied configurations.

It thus appears that in a complex case as the selected one, numerical simulations are competitive with wind tunnel evaluations only if economy is made on the number of considered attack angles and/or, length of the time-histories and configurations (we remind that in wind tunnel tests actually two configurations have been tested with a 10° stepping). On the other side, when it is possible to study a reduced number of incidence angles (e.g. due to symmetry) or due to the expected structural behaviour, CFD already appears as an optimal choice, although carefulness has to be used in evaluating local peak pressures.

6. Conclusions

In the present paper, the recently designed Torre Gioia 22 has been selected as case study for the evaluation of the wind loads based on CFD simulations. The analyses showed a good capability of numerical simulations to reproduce wind tunnel tests, being the most important source of discrepancy the difficulty encountered in numerical simulations in the reproduction of extreme suctions. Local refinements in the immediate proximity of the

building surfaces were able to alleviate the problem but not to eliminate such effects, which probably require a finer mesh sizing in a wider zone close to the building, so remarkably increasing the computational costs.

In particular, we remark that mesh sizing and numerical schemes which, in the authors' experience, provide a reasonable compromise between accuracy, computational cost and numerical stability have been reported. Such settings are indeed problem dependent and well-adapted to sharp-edged bluff bodies immersed in mildly and highly turbulent flows. In particular we here recall:

1. the mesh size here adopted in the proximity of the studied structure has size comprised between $0.01H_r$ and $0.005H_r$ being H_r the object characteristic scale. In the authors' experience, the addition of boundary layer cells is often found to be very costly (especially due to the consequent requirements in terms of stable time step) and often unnecessary;
2. the use of partially-corrected schemes can be used in order to increase the computations stability. Although suboptimal such choice is often unavoidable and leads to acceptable results;
3. as it is well-known, the synthetic inflow can be generated by various available methods. The authors briefly reported the factors which, in their experience, mainly contribute to their success and led to the development of the PRFG[3] here adopted;
4. the fact that synthetic inflows inevitably lead to the insurgence of spurious pressure fluctuations (at least due to incompatibility with other boundary conditions) at the inflow has been discussed and the VBIC procedure used to alleviate such effect.

Finally, the computational cost of such simulations is analysed. It appears that at the current stage, the cost of running accurate numerical simulations is still comparable, if not higher, than wind tunnel tests. This is particularly true in the case of complex surroundings or multiple design scenarios. However, the use of numerical simulations appears to be already well-suited for cases in which it is possible to define *a priori* a limited number of conditions to be tested.

As a result, while it is not difficult to foresee a future in which numerical simulations will overtake wind tunnel tests, the two techniques currently appear optimal in different conditions. Further research is still needed in order to allow a more rational use of numerical simulations: between them the use of multi-fidelity approaches and *a priori* identification of critical conditions appear to be the most promising ones.

Appendix A

As anticipated the generation of inflow conditions has been the object of numerous research works in recent years and the topic is still attracting the attention of the research community. In particular, the time-varying velocity field applied at the inflow patch must be characterized by statistics compatible with those expected on-site. It is usually assumed that turbulence intensities (one for each velocity component), time-spectra (one for each velocity component) and integral length scales (in general nine of them, three for each velocity component corresponding to the three spatial directions) provide a suitable characterization of the wind field for the purpose of wind loading evaluation.

Different synthetic turbulence generation methods often take different perspectives with respect to what target values should be adopted, although some choices can be easily shown to be equivalent. Additionally, it must be considered that the generated field must be correctly propagated inside the computational domain. Such last requirement can be fulfilled by generating velocity fields which approximate mass and momentum conservation (i.e. the divergence-free condition and Taylor assumption). Another requirement is that the generation of inflow conditions should not sensibly increment the simulation time.

With reference to the notation introduced in Sec. 4.5, within techniques of type SA, we find the full simulation of the wind tunnel arrangement and recycling methods. The use of experimental data does not require numerical simulations but it is qualitatively affine to such category. The fulfilling of Navier-Stokes equations is in this case automatic. The approach is cumbersome from the computational point of view, although the incoming flow can be generated once and than used for all attack angles and cases characterized by the same ABL type. The control of the statistics of the generated ABL is not trivial, analogously to the

disposition of roughness blocks and spires for wind tunnel tests. After calibration results are generally well satisfactory.

The category SGwo groups the majority of available synthetic turbulence generation methods. Such methods focus on the generation of synthetic flows characterized by target statistics (to be interpreted in a vast sense including time-spectra, two-point statistics, etc). The implicit assumption underlying such methods is that the synthetic field will be transmitted inside the computational domain without undergoing major modifications in order to impose the fulfillment of Navier-Stokes equations.

Historically, methods which assemble the synthetic field as a superposition of coherent structures privileged the fulfilling of Taylor assumption while methods based on Fourier synthesis privileged the fulfillment of the divergence-free conditions. The implications of such choices have been studied in detail in [37] for the case of a single velocity-wave, showing that only considering at the same time mass and momentum conservation (although linearized) allows a correct transmission of the synthetic field through the inflow patch. If the synthetic flow is built without taking such aspects into account, modifications of the velocity field at short distance from the inflow patch should be expected. Such modifications are operated by the pressure field, so leading to nonphysical pressure fluctuations. It shall be remarked that, despite pressure fluctuations, which are further commented in Appendix B, the results from these methods can be satisfactory as corrections might sometimes be small and/or do not sensibly alter the inflow characteristics. Despite the discrepancies between the targeted and the velocity fields actually transmitted through the inflow patch, good results can be often obtained after appropriate calibration.

As described above, it is convenient to generate synthetic fields characterized by both target statistical quantities and appropriate differential properties (i.e. fulfilling *a priori* approximated versions of the Navier-Stokes equations). This is required in order to allow the field to be transmitted through the inflow patch without undergoing modifications (at least with good approximation). This led to the development of SG methods. In particular, to the authors knowledge, three of the available synthetic turbulence generation methods

respect both divergence-free condition and Taylor assumption *a priori*. Two are based on the assembling of coherent structures, the DFSEM and TS methods while one, denoted as PRFG^3, proceeds by spectral synthesis. The three methods slightly differ in the specification of the target values with DFSEM and TS privileging control over the Reynolds stress tensor and PRFG^3 privileging integral length scales.

We would like to stress again that the topic is still the object of numerous researches and that acceptable results can be obtained with many of the techniques available in the literature, although for some of them an iterative optimization of the target values used for the inflow generation is necessary.

Appendix B

As previously discussed, the synthetic field might (i.e. SA) or might not (i.e. SGwo) approximate Navier-Stokes equations, depending on the adopted turbulence generation method. As anticipated, in the second case pressure fluctuations should be expected. Actually, it must be noticed that synthetic flows generally do not take into account the presence of BCs confining with the inflow patch. Such BCs require the modification of the synthetic field in the proximity of the boundaries and, thus, lead to the insurgence of pressure fluctuations in their proximity even for SG inflows. It thus appears that some nonphysical pressure fluctuations should be expected with all turbulence generation methods when the synthetic field is applied as a Dirichlet condition at the inflow. It must be also noticed that SA methods do not show such difficulties as the field imposed at the inflow is extracted from a numerical simulation which enforces Navier-Stokes and BCs.

The problem can be tackled in three different ways (here it is assumed that strong global jumps in pressure provided by global mass imbalances are prevented ensuring a constant global mass-flux through the inflow patch). Firstly, it is possible to avoid the problem simply moving the target building sufficiently far from the inflow [27]. The second possibility is to apply velocity at cell centres in a plane located slightly downstream the inflow patch in the predictor step of the pressure-velocity coupling algorithm [38]. Recently, a procedure able to allow to impose the synthetic field at the inflow patch as a standard Dirichlet BC without

causing nonphysical pressure fluctuations has been proposed in [33]. The method, denoted as VBIC, allows to correct the synthetic inflow enforcing the divergence-free condition and accounting for the presence of BCs. The corrections are built in order to be of minimal norm over the inflow patch.

Acknowledgments

The authors are thankful to CINECA for providing the HPC facilities which allowed the completion of the present study. The support provided by China Scholarship Council (CSC) is acknowledged.

References

[1] B. Blocken, "50 years of computational wind engineering: past, present and future," Journal of Wind Engineering and Industrial Aerodynamics, vol. 129, pp. 69–102, 2014.

[2] Y. Tamura and P. Van Phuc, "Development of CFD and applications: Monologue by a non-CFD-expert," Journal of Wind Engineering and Industrial Aerodynamics, vol. 144, pp. 3–13, 2015.

[3] X. Zhao, W. Liu, D. Lai, and Q. Chen, "Optimal design of an indoor environment by the CFD-based adjoint method with area-constrained topology and cluster analysis," Building and Environment, vol. 138, pp. 171–180, 2018.

[4] X. Zhang, K. T. Tse, A. U. Weerasuriya, K. Kwok, J. Niu, Z. Lin, and C. M. Mak, "Pedestrian-level wind conditions in the space underneath lift-up buildings," Journal of Wind Engineering and Industrial Aerodynamics, vol. 179, pp. 58–69, 2018.

[5] C. García-Sánchez, G. Van Tendeloo, and C. Gorlé, "Quantifying inflow uncertainties in RANS simulations of urban pollutant dispersion," Atmospheric Environment, vol. 161, pp. 263–273, 2017.

[6] C. García-Sánchez, J. van Beeck, and C. Gorlé, "Predictive large eddy simulations for urban flows: Challenges and opportunities," Building and Environment, vol. 139, pp. 146–156, 2018.

[7] A. Dagnew and G. T. Bitsuamlak, "Computational evaluation of wind loads on buildings: a review," Wind Struct, vol. 16, no. 6, pp. 629–660, 2013.

[8] M. S. Thordal, J. C. Bennetsen, S. Capra, A. K. Kragh, and H. H. H. Koss, "Towards a standard CFD setup for wind load assessment of high-rise buildings: Part 2–blind test of chamfered and rounded corner high-rise buildings," Journal of Wind Engineering and Industrial Aerodynamics, vol. 205, p. 104282, 2020.

[9] Y. Wang and X. Chen, "Simulation of approaching boundary layer flow and wind loads on high-rise buildings by wall-modeled LES," Journal of Wind Engineering and Industrial Aerodynamics, vol. 207, p. 104410, 2020.

[10] G. Lamberti and C. Gorlé, "Sensitivity of LES predictions of wind loading on a high-rise building to the inflow boundary condition," Journal of Wind Engineering and Industrial Aerodynamics, vol. 206, p. 104370, 2020.

[11] J. Wang, Q. Yang, P. Van Phuc, and Y. Tamura, "Characteristics of conical vortices and their effects on wind pressures on flat-roof-mounted solar arrays by LES," Journal of Wind Engineering and Industrial Aerodynamics, vol. 200, p. 104146, 2020.

[12] G. Schewe, "Sensitivity of transition phenomena to small perturbations in flow round a circular cylinder," Journal of fluid mechanics, vol. 172, pp. 33–46, 1986.

[13] B. Rocchio, A. Mariotti, and M. Salvetti, "Flow around a 5: 1 rectangular cylinder: Effects of upstream-edge rounding," Journal of Wind Engineering and Industrial Aerodynamics, vol. 204, p. 104237, 2020.

[14] I. Celik, Z. Cehreli, and I. Yavuz, "Index of resolution quality for large eddy simulations," 2005.

[15] M. S. Thordal, J. C. Bennetsen, S. Capra, and H. H. H. Koss, "Towards a standard CFD setup for wind load assessment of high-rise buildings: Part 1–benchmark of the caarc building," Journal of Wind Engineering and Industrial Aerodynamics, vol. 205, p. 104283, 2020.

[16] F. Xing, D. Mohotti, and K. Chauhan, "Study on localised wind pressure development in gable roof buildings having different roof pitches with experiments, RANS and LES simulation models," Building and Environment, vol. 143, pp. 240–257, 2018.

[17] J. Wang, P. Van Phuc, Q. Yang, and Y. Tamura, "LES study of wind pressure and flow characteristics of flat-roof-mounted solar arrays," Journal of Wind Engineering and Industrial Aerodynamics, vol. 198, p. 104096, 2020.

[18] X. Zheng, H. Montazeri, and B. Blocken, "CFD simulations of wind flow and mean surface pressure for buildings with balconies: Comparison of RANS and LES," Building and Environment, vol. 173, p. 106747, 2020.

[19] P. V. Phuc, T. Nozu, H. Kikuchi, K. Hibi, and Y. Tamura, "Wind pressure distributions on buildings using the coherent structure smagorinsky model for LES," Computation, vol. 6, no. 2, p. 32, 2018.

[20] T. Nozu, T. Tamura, K. Takeshi, and K. Akira, "Mesh-adaptive LES for wind load estimation of a high-rise building in a city," Journal of Wind Engineering and Industrial Aerodynamics, vol. 144, pp. 62–69, 2015.

[21] A. Cimarelli, A. Leonforte, and D. Angeli, "Direct numerical simulation of the flow around a rectangular cylinder at a moderately high reynolds number," Journal of Wind Engineering and Industrial Aerodynamics, vol. 174, pp. 39–49, 2018.

[22] A. Yoshizawa, "Statistical theory for compressible turbulent shear flows, with the application to subgrid modeling," The Physics of fluids, vol. 29, no. 7, pp. 2152–2164, 1986.

[23] H. Weller, "Controlling the computational modes of the arbitrarily structured C grid," Monthly Weather Review, vol. 140, no. 10, pp. 3220–3234, 2012.

[24] Eurocode, "Eurocode 1: Actions on structures," 2009.

[25] ESDU, "Characteristics of atmospheric turbulence near the ground," Engineering Sciences Data Unit, IHS Group, 2001.

[26] G. Solari, "Gust buffeting. i: Peak wind velocity and equivalent pressure," Journal of Structural Engineering, vol. 119, no. 2, pp. 365–382, 1993.

[27] M. Bervida and L. Patruno, "Synthetic generation of the atmospheric boundary layer for wind loading assessment using spectral methods," Journal of Wind Engineering and Industrial Aerodynamics, vol. 196, p. 104040, 2020.

[28] C. Dyrbye and S. O. Hansen, Wind loads on structures. John Wiley and Sons Inc, 1997.

[29] J. D. Holmes, Wind loading of structures. CRC press, 2018.

[30] X. Wu, "Inflow turbulence generation methods," Annual Review of Fluid Mechanics, vol. 49, pp. 23–49, 2017.

[31] C. Mockett, H. Werner, and D. Schwamborn, Go4Hybrid: Grey Area Mitigation for Hybrid RANS-LES Methods. Springer-Verlag, 2018.

[32] L. Patruno and M. Ricci, "A systematic approach to the generation of synthetic turbulence using spectral methods," Computer Methods in Applied Mechanics and Engineering, vol. 340, pp. 881–904, 2018.

[33] L. Patruno and S. de Miranda, "Unsteady inflow conditions: A variationally based solution to the insurgence of pressure fluctuations," Computer Methods in Applied Mechanics and Engineering, vol. 363, p. 112894, 2020.

[34] CNR, "CNR-DT 207 R1/2018: Istruzioni per la valutazione delle azioni e degli effetti del vento sulle costruzioni," 2018.

[35] Rescale, "The real cost of high performance computing." https://resources.rescale.com/, 2020 (accessed: 15,12,2020).

[36] E. Walker, "The real cost of a CPU hour," Computer, vol. 42, no. 4, pp. 35–41, 2009.

[37] L. Patruno and M. Ricci, "On the generation of synthetic divergence-free homogeneous anisotropic turbulence," Computer Methods in Applied Mechanics and Engineering, vol. 315, pp. 396–417, 2017.

[38] Y. Kim, I. P. Castro, and Z.-T. Xie, "Divergence-free turbulence inflow conditions for large-eddy simulations with incompressible flow solvers," Computers & Fluids, vol. 84, pp. 56–68, 2013.